Journal of Computational Physics **172,** 40–70 (2001)
doi:10.1006/jcph.2001.6754, available online at http://www.idealibrary.com on IDEAL®

Stability of Pressure Boundary Conditions for Stokes and Navier–Stokes Equations

N. Anders Petersson

Center for Applied Scientific Computing, Lawrence Livermore National Laboratory, Livermore, California 94550
E-mail: andersp@llnl.gov

Received April 26, 2000; revised January 4, 2001

The stability of a finite difference discretization of the time-dependent incompressible Navier–Stokes equations in velocity-pressure formulation is studied. In paticular, we compare the stability for different pressure boundary conditions in a semiimplicit time-integration scheme. where only the viscous term is treated implicitly. The stability is studied in three different ways: by a normal-mode analysis, by numerical computation of the amplification factors, and by direct numerical simulation of the governing equations. All three approaches identify the same pressure boundary condition as the best alternative. This condition implicitly enforces the normal derivative of the divergence to be zero on the boundary by coupling the normal derivative of the pressure to the normal component of the curl of the vorticity. Using this boundary condition, we demonstrate that the time-step is determined only by the convective term.

Key Words: incompressible Navier–Stokes; velocity-pressure formulation; normal-mode analysis; chimera grids.

1. INTRODUCTION

We consider the stability of a finite difference discretization of the time-dependent incompressible Navier–Stokes equations in velocity-pressure formulation. In particular, we are interested in a semi-implicit time-integration scheme, where the convective term is handled explicitly and the viscous term is treated implicitly. Similar to a projection method [1], the velocity-pressure formulation makes it possible to split the computation of the pressure from the computation of the velocity. But in order to do so, a boundary condition for the pressure must be specified (unless a staggered grid is used [8]). The accuracy of various alternatives has been studied extensively in the literature [3], but numerical computations indicate that the stability is also affected by the specific choice of pressure boundary condition, in particular for a semi-implicit method. In this paper, we perform a detailed

0021-9991/01 $35.00

TABLE I
The Three Pressure Boundary Conditions

div–grad	$\dfrac{\partial p}{\partial n} = \nu \boldsymbol{n} \cdot \nabla^2 \boldsymbol{u} + \boldsymbol{n} \cdot \boldsymbol{f}$
	$\nabla \cdot \boldsymbol{u} = 0$
curl–curl	$\dfrac{\partial p}{\partial n} = -\nu \boldsymbol{n} \cdot \nabla \times \nabla \times \boldsymbol{u} + \boldsymbol{n} \cdot \boldsymbol{f}$
coupled	$\nabla \cdot \boldsymbol{u} = 0$

study of the stability properties of three different pressure boundary conditions for no-slip walls.

For a two-dimensional domain $(x, y) \in \Omega$, the velocity-pressure formulation of the incompressible Navier–Stokes equations is

$$\begin{cases} \boldsymbol{u}_t + (\boldsymbol{u} \cdot \nabla)\boldsymbol{u} + \nabla p - \nu \nabla^2 \boldsymbol{u} = \boldsymbol{f}, & t \geq 0, \\ \nabla^2 p + \nabla u \cdot \boldsymbol{u}_x + \nabla v \cdot \boldsymbol{u}_y = \nabla \cdot \boldsymbol{f}, & t \geq 0, \\ \boldsymbol{u}(x, y, 0) = \boldsymbol{u}_0(x, y). \end{cases} \tag{1}$$

Here, $\boldsymbol{u} = (u, v)^T$ is the velocity, p is the kinematic pressure (pressure divided by the constant density), ν is the constant kinematic viscosity, and $\boldsymbol{f} = (f^{(u)}, f^{(v)})^T$ is the force per unit mass. We will focus our effort on no-slip boundaries,

$$\boldsymbol{u}(x, y, t) = 0, \quad (x, y) \in \partial\Omega, \quad t \geq 0, \tag{2}$$

and study the pressure boundary conditions stated in Table I, which we derive below.

A boundary condition for the pressure can be obtained by taking the scalar product between the momentum equations and the unit normal of the boundary, $\boldsymbol{n} = (n^{(1)}, n^{(2)})^T$. On a no-slip boundary, the condition becomes

$$\frac{\partial p}{\partial n} = \nu \boldsymbol{n} \cdot \nabla^2 \boldsymbol{u} + \boldsymbol{n} \cdot \boldsymbol{f}, \quad (x, y) \in \partial\Omega, \quad t \geq 0. \tag{3}$$

As Strikwerda [11] and Henshaw [5] point out, the pressure boundary condition (3) does not add any new information to the system since the momentum equations already are satisfied on the boundary. Thus, using (3) by itself would make the problem underdetermined.

To derive an appropriate boundary condition for the pressure, we consider the incompressible Navier–Stokes equations in velocity-divergence formulation:

$$\begin{cases} \boldsymbol{u}_t + (\boldsymbol{u} \cdot \nabla)\boldsymbol{u} + \nabla p - \nu \nabla^2 \boldsymbol{u} = \boldsymbol{f}, & t \geq 0, \\ \nabla \cdot \boldsymbol{u} = 0, & t \geq 0, \\ \boldsymbol{u}(x, y, 0) = \boldsymbol{u}_0(x, y). \end{cases} \tag{4}$$

It is straightforward to derive (1) from (4), but it is less well known under which circumstances (4) can be derived from (1), i.e., what conditions make the two systems equivalent. For this purpose, we derive an equation for the divergence, $\delta = \nabla \cdot \boldsymbol{u}$, by taking the divergence of the momentum equations in (1) and enforcing the pressure equation. This results in a homogeneous convection–diffusion equation for δ:

$$\delta_t + u\delta_x + v\delta_y - \nu \nabla^2 \delta = 0, \quad (x, y) \in \Omega, \quad t \geq 0.$$

Since (4) requires $\nabla \cdot \boldsymbol{u} = 0$ for $t \geq 0$, the initial velocity field must also be divergence free: $\nabla \cdot \boldsymbol{u}_0 = 0$. Hence, the divergence can only depart from zero if it becomes nonzero on the boundary $\partial\Omega$. Therefore, one alternative for making the velocity-pressure and velocity-divergence formulations equivalent is to enforce

$$\nabla \cdot \boldsymbol{u} = 0, \quad (x, y) \quad \text{on } \partial\Omega, \quad t \geq 0. \tag{5}$$

In the spatially discretized problem, boundary condition (5) is used to eliminate the ghost point value of the velocity from the right-hand side of the Neumann condition (3). The boundary condition (3), (5) will be referred to as the div–grad condition.

While the div–grad condition works fine in an explicit scheme (see Henshaw [5]), it does not perform as well in our proposed semi-implicit method. Here, we have observed that the time-step needs to be much smaller than what a von Neumann analysis indicates in order for the scheme to be stable.

As an alternative to the Dirichlet condition (5), we can make the velocity-divergence and velocity-pressure formulations equivalent by prescribing the normal derivative of the divergence to be zero on the boundary:

$$\frac{\partial \delta}{\partial n} \equiv \boldsymbol{n} \cdot \nabla \delta = 0, \quad (x, y) \quad \text{on } \partial\Omega, \quad t \geq 0. \tag{6}$$

By using the identity

$$\Delta \boldsymbol{u} = \nabla(\nabla \cdot \boldsymbol{u}) - \nabla \times \nabla \times \boldsymbol{u},$$

the term $\boldsymbol{n} \cdot \Delta \boldsymbol{u}$ in the pressure boundary condition (3) can be written

$$\boldsymbol{n} \cdot \Delta \boldsymbol{u} = \boldsymbol{n} \cdot \nabla \delta - \boldsymbol{n} \cdot (\nabla \times \nabla \times \boldsymbol{u}).$$

Hence, we can build the condition $\partial\delta/\partial n = 0$ into the pressure boundary condition (3) by enforcing

$$\frac{\partial p}{\partial n} = -\nu \boldsymbol{n} \cdot (\nabla \times \nabla \times \boldsymbol{u}) + \boldsymbol{n} \cdot \boldsymbol{f}, \quad (x, y) \in \partial\Omega, \quad t \geq 0. \tag{7}$$

We will call this the curl–curl condition. This boundary condition has been used before; see for example Karniadakis *et al.* [7], who studied the accuracy of split velocity-pressure methods in the context of spectral element discretizations. However, no analysis of the stability was supplied.

A third, more expensive, alternative is to solve the pressure equation together with the momentum equations. Then, no explicit boundary condition for the pressure is needed and it suffices to enforce (5), i.e., the divergence of the velocity to be zero on the boundary. We call this the coupled condition. We remark that this approach defies the basic motivation for using the velocity-pressure formulation since it requires the pressure and momentum equations to be solved simultaneously. If one is willing to do that, one could instead consider solving the Navier–Stokes equations in velocity-divergence formulation; see Strikwerda [12] for example.

To analyze the stability of the three aforementioned boundary conditions, we consider Stokes equations in velocity-pressure formulation. Even though this problem lacks the

nonlinear convective term in Navier–Stokes equations, it retains the difficulty of making the velocity-pressure and the velocity-divergence formulations equivalent, i.e., enforcing the divergence of the velocity to be zero on the boundary.

The remainder of the paper is organized as follows. In Section 2, we perform a normal-mode analysis to study the stability of the semidiscrete Stokes equations for a half-plane problem where time is left continuous. Here all three boundary conditions are shown to satisfy the eigenvalue condition, which is necessary for stability. In Section 3, we extend the normal-mode analysis to the fully discrete case, where the backwards Euler method is used to discretize time. Even though this method is only first-order accurate in time, it clearly demonstrates the stability properties of the various boundary conditions. We show that the div–grad condition yields an unstable scheme for time-steps $\Delta t > Ch^2$, where h is the grid size and C is a constant. The other two boundary conditions satisfy the necessary Godunov–Ryabenkii condition [4] for all $\Delta t > 0$. We proceed in Section 4 by numerically computing the amplification factors for a periodic channel domain. First, we consider Stokes equations, where the theoretical results for the backwards Euler method are confirmed. We continue by studying the linearized Navier–Stokes equations, where the viscous term is handled implicitly and the convective term explicitly. Again, the div–grad condition is shown to have inferior stability properties compared with the other two boundary conditions. Finally, in Section 5, we apply the theory to compute unsteady flow around circular cylinders. We perform the calculations on an overlapping grid with a second-order accurate semi-implicit time-integration scheme. Both the div–grad and the curl–curl conditions are tested as well as a simple homogeneous Neumann condition for the pressure. We conclude that the stability of the div–grad condition is inferior, and that the accuracy of the simple homogeneous Neumann condition is poor, compared to the curl–curl condition (7).

2. THE SEMIDISCRETE CASE

As a model for the incompressible Navier–Stokes equations, we consider Stokes equations. In this section we leave time continuous, but discretize by second-order accurate centered divided differences in space. We will study the semiinfinite domain $y \geq 0$ for 2π-periodic functions in x. A uniform Cartesian grid is employed with the step size $\Delta x = \Delta y = h = 2\pi/N$. The grid points are given by $x_j = (j-1)h$, $j = 1, 2, \ldots, N$; $y_k = (k-1)h$, $k = 0, 1, 2, \ldots$. We denote a grid function by $f_{j,k} = f(x_j, y_k)$ and define the one-sided and centered divided difference operators by

$$D_+^y f_{j,k} = \frac{f_{j,k+1} - f_{j,k}}{\Delta y}, \quad D_-^y f_{j,k} = D_+^y f_{j,k-1}, \quad D_0^y = \frac{1}{2}(D_+^y + D_-^y),$$

and corresponding expressions for the divided difference operators in the x-direction.

At $y = 0$, we impose the no-slip boundary condition: $\boldsymbol{u}(x, 0, t) = 0$. For the pressure, we will examine the three aforementioned boundary conditions. After discretization, the coupled condition becomes

$$D_0^y v = 0, \quad y = 0. \tag{8}$$

The div–grad condition is given by

$$\begin{cases} D_0^y p = D_+^y D_-^y v, \\ D_0^y v = 0, \end{cases} \quad y = 0,$$

which can be written

$$D_0^y p = \frac{2}{h} D_+^y v, \quad y = 0.$$

Finally, the curl–curl condition is

$$D_0^y p = -D_0^x D_0^y u, \quad y = 0.$$

For convenience, we write all pressure boundary conditions in the form

$$A^{(q)} D_0^y p = B^{(q)} \boldsymbol{u}, \quad y = 0, \tag{9}$$

for $q = 1, 2,$ or 3. The coupled condition has $A^{(1)} = 0$ and $B^{(1)}\boldsymbol{u} = D_0^y v$; the div–grad condition corresponds to $A^{(2)} = 1$ and $B^{(2)}\boldsymbol{u} = \frac{2}{h} D_+^y v$. Finally, the curl–curl condition has $A^{(3)} = 1$ and $B^{(3)}\boldsymbol{u} = D_0^x D_0^y u$.

With this notation, the discretized Stokes equations are (omitting the grid point index)

$$\begin{aligned}
u_t + D_0^x p &= D_+^x D_-^x u + D_+^y D_-^y u + f^{(u)}, \\
v_t + D_0^y p &= D_+^x D_-^x v + D_+^y D_-^y v + f^{(v)}, \\
D_+^x D_-^x p + D_+^y D_-^y p &= D_0^x f^{(u)} + D_0^y f^{(v)} := f^{(p)}, \\
\boldsymbol{u}(x, 0, t) &= 0, \\
A^{(q)} D_0^y p(x, 0, t) &= B^{(q)} \boldsymbol{u}(x, 0, t), \quad q = 1, 2, \text{ or } 3, \\
\boldsymbol{u}(x, y, 0) &= 0, \\
p(x, y, 0) &= 0.
\end{aligned} \tag{10}$$

Note that the assumption of homogeneous initial data is not a restriction but is motivated by the use of the Laplace transform method to analyze the stability. A problem with inhomogeneous initial data $\boldsymbol{u}(x, y, 0) = \boldsymbol{u}_0(x, y)$ can be transformed to a problem with homogeneous initial data by the change of variables $\tilde{\boldsymbol{u}}(x, y, t) = \boldsymbol{u}(x, y, t) - q(t)\boldsymbol{u}_0(x, y)$, where $q(t)$ is a smooth function with $q(0) = 1$.

We denote the discrete Fourier transform of a grid function $f(x_j, y_k)$ that is 2π-periodic in the x-direction by

$$f(x_j, y_k) = \frac{1}{\sqrt{2\pi}} \sum_{\omega=0}^{N-1} \tilde{f}(\omega, y_k) \exp(i\omega x_j).$$

To analyze the stability, we Fourier-transform the solution in the x-direction and Laplace-transform in time. The dual variables of $\boldsymbol{u}(x, y, t)$ and $p(x, y, t)$ are denoted by $\hat{\boldsymbol{u}}(\omega, y, s)$ and $\hat{p}(\omega, y, s)$, respectively. The transformed counterpart of (10) is

$$\begin{aligned}
s\hat{u} + \frac{i}{h} \sin(\omega h)\hat{p} &= -\frac{4}{h^2} \sin^2(\omega h/2)\hat{u} + D_+^y D_-^y \hat{u} + \hat{f}^{(u)}, \\
s\hat{v} + D_0^y \hat{p} &= -\frac{4}{h^2} \sin^2(\omega h/2)\hat{v} + D_+^y D_-^y \hat{v} + \hat{f}^{(v)}, \\
-\frac{4}{h^2} \sin^2(\omega h/2)\hat{p} + D_+^y D_-^y \hat{p} &= \hat{f}^{(p)}, \\
\hat{\boldsymbol{u}}(\omega, 0, s) &= 0, \\
A^{(q)} D_0^y \hat{p}(\omega, 0, s) &= \hat{B}^{(q)} \hat{\boldsymbol{u}}(\omega, 0, s), \quad q = 1, 2, \text{ or } 3.
\end{aligned}$$

Here $\hat{B}^{(q)}$ is the Fourier-transformed counterpart of $B^{(q)}$. We consider the wave numbers $\omega = 0, 1, \ldots, N-1$, which correspond to a complete set of eigenfunctions $e^{i\omega x}$ on the grid.

It is shown in Gustafsson *et al.* [4] that the stability properties of (10) are closely related to the eigenvalue problem

$$\begin{aligned} s\hat{u} + \frac{i}{h}\sin(\omega h)\hat{p} &= -\frac{4}{h^2}\sin^2(\omega h/2)\hat{u} + D_+^y D_-^y \hat{u}, \\ s\hat{v} + D_0^y \hat{p} &= -\frac{4}{h^2}\sin^2(\omega h/2)\hat{v} + D_+^y D_-^y \hat{v}, \\ -\frac{4}{h^2}\sin^2(\omega h/2)\hat{p} + D_+^y D_-^y \hat{p} &= 0, \\ \hat{\boldsymbol{u}}(\omega, 0, s) &= 0, \\ A^{(q)} D_0^y \hat{p}(\omega, 0, s) &= \hat{B}^{(q)}\hat{\boldsymbol{u}}(\omega, 0, s), \quad q = 1, 2, \text{ or } 3. \end{aligned} \tag{11}$$

We call s an eigenvalue if there is a nontrivial solution of (11) with bounded L_2-norm.

Several stability definitions for difference approximations are possible and we refer to [4] for a discussion. Clearly, the solution cannot be stable if there is an eigenvalue with $\Re(s) > 0$, since it would correspond to an exponential growth in time of the original variables. Norm estimates in terms of the original variables can often be obtained if there are no eigenvalues in $\Re(s) \geq 0$ for the Fourier–Laplace transformed problem (see [4]), but we postpone this analysis to a subsequent paper. Here, we will only check if there are eigenvalues in $\Re(s) \geq 0$.

The pressure equation in (11) is solved by $\hat{p}(y) = Pe^{-\alpha y}$, where $\alpha \geq 0$ satisfies

$$\sinh\left(\frac{\alpha h}{2}\right) = \sin\left(\frac{\omega h}{2}\right). \tag{12}$$

Inserting $\hat{p}$ into (11) yields

$$D_+^y D_-^y \hat{u} - \left(s + \frac{4}{h^2}\sin^2\left(\frac{\omega h}{2}\right)\right)\hat{u} = \frac{i}{h}\sin(\omega h)Pe^{-\alpha y}, \tag{13}$$

$$D_+^y D_-^y \hat{v} - \left(s + \frac{4}{h^2}\sin^2\left(\frac{\omega h}{2}\right)\right)\hat{v} = -\frac{1}{h}\sinh(\alpha h)Pe^{-\alpha y}. \tag{14}$$

The homogeneous part of these equations is the same and is solved by $\hat{u}_h(y) = e^{-\beta y}$, where β is the solution of

$$\frac{4}{h^2}\sinh^2\left(\frac{\beta h}{2}\right) = s + \frac{4}{h^2}\sin^2\left(\frac{\omega h}{2}\right), \quad \Re(\beta) > 0. \tag{15}$$

The particular solution has the form $\hat{u}_p(y) = Ae^{-\alpha y}$. Inserting this expression into (13) and identifying the coefficients yields

$$A = \frac{\frac{i}{h}\sin(\omega h)P}{\frac{4}{h^2}\sinh^2(\alpha h/2) - \left(s + \frac{4}{h^2}\sin^2(\omega h/2)\right)} = -\frac{i}{hs}\sin(\omega h)P.$$

Enforcing the boundary condition $\hat{\boldsymbol{u}}(\omega, 0, s) = 0$ gives the solution to (11):

$$\hat{u}(y) = -\frac{i\,P\sin(\omega h)}{hs}(e^{-\alpha y} - e^{-\beta y}), \tag{16}$$

$$\hat{v}(y) = \frac{P\sinh(\alpha h)}{hs}(e^{-\alpha y} - e^{-\beta y}), \tag{17}$$

$$\hat{p}(y) = Pe^{-\alpha y}. \tag{18}$$

The remaining coefficient P must be determined by the last equation in (11) and we proceed by analyzing the various cases.

2.1. The Coupled Condition

The boundary condition $D_0^y \hat{v}(\omega, 0, s) = 0$ gives

$$P\frac{\sinh(\alpha h)}{hs}\left(\frac{\sinh(\beta h)}{h} - \frac{\sinh(\alpha h)}{h}\right) = 0. \tag{19}$$

For $\omega = 0$, which corresponds to $\alpha = 0$, there is a nontrivial solution P. This corresponds to the undetermined constant in the pressure which can be fixed by enforcing the mean of the pressure to be zero. We proceed by studying $\omega > 0$ and introduce

$$q(s) = \frac{1}{s}(\sinh(\beta(s)h) - \sinh(\alpha h)). \tag{20}$$

An example of the function $q(s)$ is shown in Fig. 1. We have

LEMMA 2.1. *The function $q(s)$ satisfies $q(s) \neq 0$ for $\Re(s) \geq 0$.*

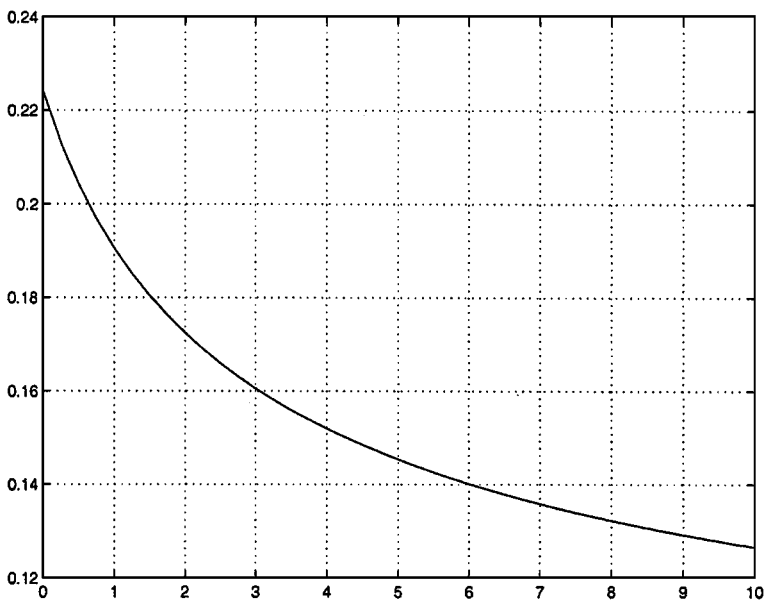

FIG. 1. The function $q(s)$ for real-valued s for the case $n = 15$, $\omega = 1$.

Proof. From the definition of $\beta(s)$,

$$\sinh\left(\frac{\beta(s)h}{2}\right) = \sqrt{\frac{h^2 s}{4} + \sin^2\left(\frac{\omega h}{2}\right)}.$$

Hence, the double angle formula yields

$$\begin{aligned}\sinh(\beta h) &= 2\sinh(\beta h/2)\sqrt{1+\sinh^2(\beta h/2)} \\ &= 2\sqrt{h^2 s/4 + \sin^2(\omega h/2)}\sqrt{1 + h^2 s/4 + \sin^2(\omega h/2)}. \end{aligned} \tag{21}$$

Further, $\alpha = \beta(0)$, so $q(s)$ can only be zero if

$$\sinh(\beta(s)h) = \sinh(\alpha h).$$

Inserting the double angle formulas gives

$$\left(\frac{h^2 s}{4} + \sin^2(\omega h/2)\right)\left(1 + \frac{h^2 s}{4} + \sin^2(\omega h/2)\right) = \sin^2(\omega h/2)(1+\sin^2(\omega h/2)),$$

which has one root at $s = 0$ and one at $s = -4(1+2\sin^2(\omega h/2))/h^2$. However, at $s = 0$, the denominator of $q(s)$ is also zero. By using l'Hospital's rule, we get

$$\begin{aligned}\lim_{s\to 0} q(s) &= h\cosh(\beta(0)h)\left.\frac{d\beta}{ds}\right|_{s=0} = \frac{\cosh(\alpha h)h^2}{4\sinh(\alpha h/2)\sqrt{1+\sinh^2(\alpha h/2)}} \\ &= \frac{\cosh(\alpha h)h^2}{2\sinh(\alpha h)} = \frac{h^2}{2\tanh(\alpha h)}. \end{aligned} \tag{22}$$

Hence $q(s) > 0$ for all $\Re(s) \geq 0$. This proves the lemma.

We conclude that the system (11) with the boundary condition $D_0^y \hat{v}(\omega, 0, s) = 0$ does not have any eigenvalues in $\Re(s) \geq 0$.

In subsequent sections, we will need the following lemma.

LEMMA 2.2. *The function $q(s)$ satisfies $\Im(q(s)) = 0$ if and only if $\Im(s) = 0$.*

Proof. If the imaginary part of $q(s)$ is zero, $q(s)$ must be real-valued; so there is a real-valued constant C such that

$$q(s) = \frac{1}{s}\left(\sinh(\beta(s)h) - \sinh(\alpha h)\right) = C.$$

Hence,

$$(\sinh(\alpha h) + Cs)^2 = \sinh^2(\beta(s)h).$$

After inserting the expressions for α and $\beta(s)$, we get

$$C^2 s^2 + 4Cs\sin(\omega h/2)\sqrt{1+\sin^2(\omega h/2)} = \frac{h^4 s^2}{4} + h^2 s(1+2\sin^2(\omega h/2)).$$

One root is $s = 0$, and since C is real-valued, the other root is also real-valued. Hence, all solutions of $\Im(q(s)) = 0$ have $\Im(s) = 0$. This proves the lemma.

We also have

LEMMA 2.3. *The imaginary part of $q(s)$ is negative for $\Im(s) > 0$ and positive for $\Im(s) < 0$.*

Proof. For imaginary s, $s = i\epsilon$, we have

$$q(i\epsilon) = -\frac{2i}{\epsilon}\left(\sqrt{a + \epsilon b + \epsilon^2 c} - \sqrt{a}\right),$$

where

$$\begin{aligned} a &= \sin^2(\omega h/2)(1 + \sin^2(\omega h/2)), \\ b &= \frac{h^2 i}{4}(1 + 2\sin^2(\omega h/2)), \\ c &= -\frac{h^4}{16}. \end{aligned}$$

For $0 < \epsilon \ll 1$, an expansion yields

$$q(i\epsilon) = -\frac{ib}{\sqrt{a}} - \frac{i\epsilon}{4a\sqrt{a}}(4ac - b^2) + O(\epsilon^2).$$

Since b is purely imaginary, the first term is real, and after some algebra,

$$4ac - b^2 = \frac{h^4}{16},$$

so

$$\Im(q(i\epsilon)) = -\frac{\epsilon h^4}{64a\sqrt{a}} + O(\epsilon^2) < 0, \quad 0 < \epsilon \ll 1.$$

Since $\Im(q(s)) \neq 0$ for $\Im(s) \neq 0$ and $q(s)$ is continuous, we have $\Im(q(s)) < 0$ for $\Im(s) > 0$. Further, $q(\overline{s}) = \overline{q(s)}$, so $\Im(q(s)) > 0$ for $\Im(s) < 0$. This proves the lemma.

2.2. The Div–Grad Condition

The boundary condition $D_0^y \hat{p}(\omega, 0, s) = \frac{2}{h} D_+^y \hat{v}(\omega, 0, s)$ gives

$$-P\frac{\sinh(\alpha h)}{h} = \frac{2P\sinh(\alpha h)}{h^3 s}(e^{-\alpha h} - e^{-\beta h}),$$

which can be written

$$P\frac{\sinh(\alpha h)}{h}\left(1 + \frac{2(e^{-\alpha h} - e^{-\beta h})}{h^2 s}\right) = 0.$$

We remark that it is not necessary to analyze this case since $D_0^y \hat{p} = \frac{2}{h} D_+^y \hat{v}$ is equivalent to the coupled condition $D_0^y \hat{v} = 0$. To see this, we note that the v-equation in (11) reduces to $D_0^y \hat{p} = D_+^y D_-^y \hat{v}$ on $y = 0$. Hence $D_+^y D_-^y \hat{v} = \frac{2}{h} D_+^y \hat{v}$, which gives $D_0^y \hat{v} = 0$.

2.3. The Curl–Curl Condition

The boundary condition $D_0^y \hat{p}(\omega, 0, s) = -\frac{i}{h}\sin(\omega h) D_0^y \hat{u}(\omega, 0, s)$ leads to

$$P\left(\frac{\sinh(\alpha h)}{h} - \frac{\sin^2(\omega h)}{h^2 s}\left(\frac{\sinh(\beta h)}{h} - \frac{\sinh(\alpha h)}{h}\right)\right) = 0. \tag{23}$$

Similar to the two previous boundary conditions, this also allows for nontrivial solutions for $\omega = 0$ that are due to the undetermined constant in the pressure. We proceed by considering $\omega > 0$. Here we study

$$q_2(s) = h^2 \sinh(\alpha h) - \sin^2(\omega h) q(s). \tag{24}$$

By Lemma 2.2 it follows that $\Im(q_2(s)) = 0$ if and only if $\Im(s) = 0$. Hence, we only need to consider real-valued s and we proceed by studying $q_2(s)$ for $s = \xi$, $\Im(\xi) = 0$. We note that by (22),

$$\lim_{\xi \to 0} q_2(\xi) = h^2 \sinh(\alpha h) - \sin^2(\omega h)\frac{h^2}{2\tanh(\alpha h)}.$$

In order to show that $q_2(\xi) > 0$ for $\xi \geq 0$ we need the following lemmas.

LEMMA 2.4. *The function $q_2(\xi)$ satisfies $q_2(0) > 0$.*

Proof. We have

$$q_2(0) = \frac{h^2}{\sinh(\alpha h)}\left(\sinh^2(\alpha h) - \frac{\sin^2(\omega h)\cosh(\alpha h)}{2}\right).$$

The appropriate double angle formulas and (12) give

$$\begin{aligned}
\cosh(\alpha h) &= 1 + 2\sinh^2\left(\frac{\alpha h}{2}\right),\\
\sinh^2(\alpha h) &= 4\sinh^2\left(\frac{\alpha h}{2}\right)\left(1 + \sinh^2\left(\frac{\alpha h}{2}\right)\right),\\
\sin^2(\omega h) &= 4\sinh^2\left(\frac{\alpha h}{2}\right)\left(1 - \sinh^2\left(\frac{\alpha h}{2}\right)\right).
\end{aligned}$$

Hence,

$$\begin{aligned}
q_2(0) &= \frac{2h^2\sinh^2(\alpha h/2)}{\sinh(\alpha h)}\left[2\left(1 + \sinh^2\left(\frac{\alpha h}{2}\right)\right)\right.\\
&\quad \left. -\left(1 - \sinh^2\left(\frac{\alpha h}{2}\right)\right)\left(1 + 2\sinh^2\left(\frac{\alpha h}{2}\right)\right)\right]\\
&= \frac{2h^2\sinh^2(\alpha h/2)}{\sinh(\alpha h)}\left[1 + \sinh^2\left(\frac{\alpha h}{2}\right) + 2\sinh^4\left(\frac{\alpha h}{2}\right)\right].
\end{aligned}$$

Since all the terms on the last line are positive, $q_2(0) > 0$, which proves the lemma.

An example of the function $q_2(\xi)$ is shown in Fig. 2. We have $q_2'(\xi) = -\sin^2(\omega h) q'(\xi)$, so $q_2'(\xi)$ is positive if $q'(\xi)$ is negative. We proceed by showing

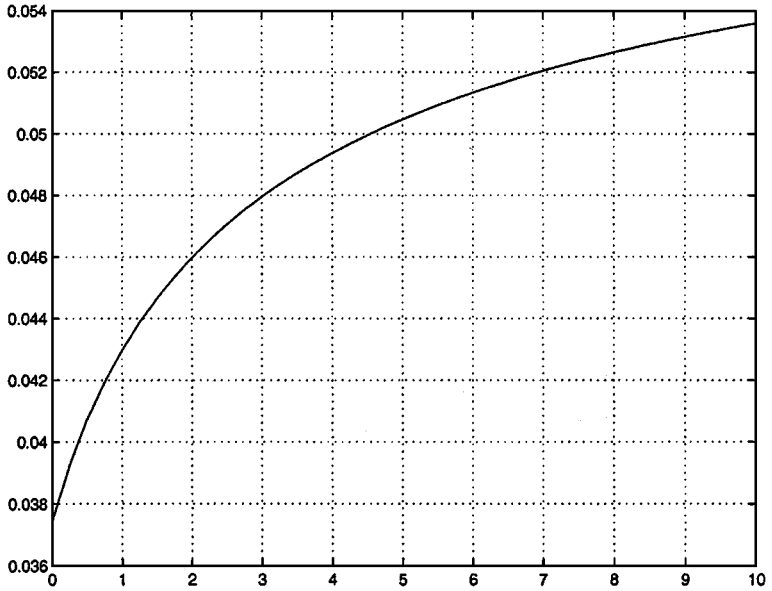

FIG. 2. The function $q_2(\xi)$ for real-valued ξ for the case $n = 15$, $\omega = 1$.

LEMMA 2.5. *The function $q(\xi)$ satisfies $q'(\xi) < 0$ for $\xi \geq 0$.*

Proof. From (21),

$$q(\xi) = -\frac{2}{\xi}\sin(\omega h/2)\sqrt{1+\sin^2(\omega h/2)} + 2\sqrt{\frac{h^4}{16} + \frac{h^2}{4\xi}(1+2\sin^2(\omega h/2)) + \frac{1}{\xi^2}\sin^2(\omega h/2)(1+\sin^2(\omega h/2))}.$$

Let us write the derivative of q as

$$q'(\xi) = \frac{-I_1(\xi) + I_2(\xi)}{N(\xi)},$$

where

$$I_1(\xi) = \frac{h^2}{4\xi^2}(1+2\sin^2(\omega h/2)) + \frac{2}{\xi^3}\sin^2(\omega h/2)(1+\sin^2(\omega h/2)),$$

$$I_2(\xi) = \frac{2}{\xi^2}\sin(\omega h/2)\sqrt{1+\sin^2(\omega h/2)}N(\xi),$$

$$N(\xi) = \sqrt{\frac{h^4}{16} + \frac{h^2}{4\xi}(1+2\sin^2(\omega h/2)) + \frac{1}{\xi^2}\sin^2(\omega g/2)(1+\sin^2(\omega h/2))}.$$

After some algebra,

$$I_1^2(\xi) - I_2^2(\xi) = \frac{h^4}{16\xi^4}.$$

Hence, $I_1^2(\xi) > I_2^2(\xi)$. Since $I_1(\xi) > 0$ and $I_2(\xi) > 0$ for $\xi > 0$, this implies $I_1(\xi) > I_2(\xi)$. Furthermore, $N(\xi) > 0$, so $q'(\xi) = (-I_1(\xi) + I_2(\xi))/N(\xi) < 0$ for $\xi > 0$. By making a

Taylor expansion of $q'(\xi)$ around $\xi = 0$, one can see that $q'(0)$ is bounded and satisfies $q'(0) < 0$. This proves the lemma.

We have proven that $q_2(0) > 0$ and that $q_2'(\xi) > 0$ for $\xi \geq 0$. Hence $q_2(\xi) > 0$ for $\xi \geq 0$, and by using Lemma 2.2 we conclude that there are no nontrivial solutions of (23) with $\Re(s) \geq 0$. Therefore, the system (11) with the boundary condition $D_0^y \hat{p}(\omega, 0, s) = -\frac{i}{h}\sin(\omega h) D_0^y \hat{u}(\omega, 0, s)$ does not have any eigenvalues in $\Re(s) \geq 0$.

3. THE FULLY DISCRETE CASE

We consider a backwards Euler discretization of the Stokes problem studied in the previous section:

$$\begin{aligned}
\frac{u^{n+1} - u^n}{\Delta t} + D_0^x p^{n+1} &= D_+^x D_-^x u^{n+1} + D_+^y D_-^y u^{n+1} + f^{(x)}, \\
\frac{v^{n+1} - v^n}{\Delta t} + D_0^y p^{n+1} &= D_+^x D_-^x v^{n+1} + D_+^y D_-^y v^{n+1} + f^{(y)}, \\
D_+^x D_-^x p^{n+1} + D_+^y D_-^y p^{n+1} &= f^{(p)}, \\
\boldsymbol{u}^n(x, 0) &= 0, \\
\boldsymbol{u}^0(x, y) &= 0, \\
p^0(x, y) &= 0.
\end{aligned} \tag{25}$$

Here, superscript n corresponds to time-level $t_n = n\Delta t$. As before, we need an additional boundary condition for the pressure and the three previously considered alternatives become

1. The coupled condition: $D_0^y v^n = 0$.
2. The div–grad condition: $D_0^y p^{n+1} = \frac{2}{h} D_+^y v^n$. Note the lagging of the velocity that is necessary in order to calculate p^{n+1} before the velocities are computed.
3. The curl–curl condition: $D_0^y p^{n+1} = -D_0^x D_0^y u^n$. Again note the lagged velocity.

To analyze the stability we make the ansatz

$$\begin{pmatrix} u^n \\ v^n \\ p^n \end{pmatrix} = \kappa^n \begin{pmatrix} u_0 \\ v_0 \\ p_0 \end{pmatrix}, \tag{26}$$

and Fourier-transform the solution in the x-direction. After setting the forcing to zero, we get the eigenvalue problem

$$\begin{aligned}
\frac{\kappa - 1}{\kappa \Delta t}\hat{u} + \frac{i}{h}\sin(\omega h)\hat{p} &= -\frac{4}{h^2}\sin^2(\omega h/2)\hat{u} + D_+^y D_-^y \hat{u}, \\
\frac{\kappa - 1}{\kappa \Delta t}\hat{v} + D_0^y \hat{p} &= -\frac{4}{h^2}\sin^2(\omega h/2)\hat{v} + D_+^y D_-^y \hat{v}, \\
-\frac{4}{h^2}\sin^2(\omega h/2)\hat{p} + D_+^y D_-^y \hat{p} &= 0, \\
\hat{\boldsymbol{u}}(\omega, 0, \kappa) &= 0, \\
A^{(q)} \kappa D_0^y \hat{p}(\omega, 0, \kappa) &= \hat{B}^{(q)} \hat{\boldsymbol{u}}(\omega, 0, \kappa), \quad q = 1, 2, \text{ or } 3.
\end{aligned} \tag{27}$$

We call κ an eigenvalue if there is a nontrivial solution of (27) with bounded L_2-norm. The Gudonov-Ryabenkii condition states that the solution of (25) is unstable if there is an eigenvalue κ of (27) with $|\kappa| > 1$. Similar to the semidiscrete case, the absence of eigenvalues with $|\kappa| > 1$ is only a necessary condition for stability. However, we postpone the analysis of sufficient conditions to a future paper. Here, we will only check if there are eigenvalues of (27) with $|\kappa| \geq 1$.

By setting $s = (\kappa - 1)/(\kappa \Delta t)$, we get the semidiscrete problem analyzed in the previous section. The solution of the first four equations in (27) is therefore

$$\hat{u}(y) = -\frac{iP\sin(\omega h)}{h}\frac{\kappa \Delta t}{\kappa - 1}(e^{-\alpha y} - e^{-\beta y}), \tag{28}$$

$$\hat{v}(y) = \frac{P\sinh(\alpha h)}{h}\frac{\kappa \Delta t}{\kappa - 1}(e^{-\alpha y} - e^{-\beta y}), \tag{29}$$

$$\hat{p}(y) = Pe^{-\alpha y}. \tag{30}$$

As in the semidiscrete case, the remaining coefficient P must be determined by the pressure boundary condition, which in this case is the last equation in (27).

Since $\kappa = 1/(1 - s\Delta t)$, $|\kappa| > 1$ corresponds to the interior of a unit circle in the complex $s\Delta t$ plane, centered at $s\Delta t = 1$. The time-step $\Delta t > 0$ can be arbitrarily small, so to make sure that there are no eigenvalues in $|\kappa| \geq 1$ for any $\Delta t > 0$ it is necessary to consider $\Re(s) > 0$ and $s = 0$. In the following we will alternate between κ and s as we find convenient.

3.1. The Coupled Condition

Since there is no lagging of time in the boundary condition $D_0^y \hat{v}(0) = 0$, we get the same problem as in the semidiscrete case for the coupled condition. Hence, there are no eigenvalues of (27) with $|\kappa| \geq 1$ for $\Delta t > 0$.

3.2. The Div–Grad Condition

The lagged velocity in the boundary condition $D_0^y p^{n+1} = \frac{2}{h} D_+^y v^n$ transforms to $\kappa D_0^y \hat{p}(0) = \frac{2}{h} D_+^y \hat{v}(0)$. Hence,

$$P\frac{\sinh(\alpha h)}{h}\left(\kappa + \frac{2(e^{-\alpha h} - e^{-\beta h})}{h^2 s}\right) = 0,$$

which is equivalent to

$$P\frac{\sinh(\alpha h)}{h}\left(\frac{1}{1 - s\Delta t} + \frac{2(e^{-\alpha h} - e^{-\beta h})}{h^2 s}\right) = 0.$$

There are nontrivial solutions if

$$q_3(s) = \frac{h^2}{1 - s\Delta t} + \frac{2(e^{-\alpha h} - e^{-\beta h})}{s}$$

becomes zero. After some numerical experiments, we found zeros of $q_3(s)$ with $\Re(s) > 0$. For example, the case $n = 15$, $\omega = 1$ is shown in Fig. 3. This example demonstrates that the boundary condition makes the scheme unstable for certain Δt.

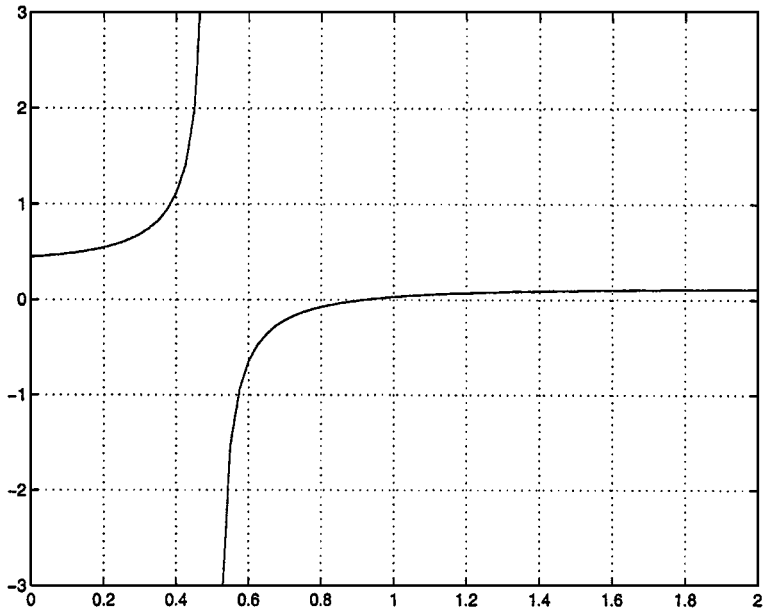

FIG. 3. The function $q_3(s)$ for real-valued s for the case $n = 15$, $\omega = 1$, and $\Delta t = 2$. Note that q_3 is unbounded at $s = 0.5$ and that it has a zero for $0.5 < s < 1$. This means that $|\kappa| > 1$, so this zero leads to an instability.

We proceed by studying $q_3(s)$ for real-valued s and set $s = \xi$, $\Im(\xi) = 0$ and study the real-valued $q_3(\xi)$ for $\xi \geq 0$. To analyze this case, we use the identity $\sinh^{-1}(\eta) = \log(\eta + \sqrt{\eta^2 + 1})$ to evaluate $e^{-\beta h}$ and $e^{-\alpha h}$:

$$q_3(\xi) = \frac{h^2}{1 - \xi \Delta t} + \frac{2}{\xi} \left(\frac{1}{\left(\sin(\omega h/2) + \sqrt{1 + \sin^2(\omega h/2)} \right)^2} - \frac{1}{\left(\sqrt{h^2 \xi/4 + \sin^2(\omega h/2)} + \sqrt{h^2 \xi/4 + \sin^2(\omega h/2) + 1} \right)^2} \right).$$

For $0 < \xi < 1/\Delta t$, $q_3(\xi)$ is clearly positive. At $\xi = 1/\Delta t$, q_3 has a pole and becomes negative for $1/\Delta t < \xi \leq 1/\Delta t + \epsilon$, $0 < \epsilon \ll 1$. On the other hand, for large ξ,

$$q_3(\xi) \sim \frac{1}{\xi} \left(-\frac{h^2}{\Delta t} + \frac{2}{\left(\sin(\omega h/2) + \sqrt{1 + \sin^2(\omega h/2)} \right)^2} \right), \quad \xi \to \infty.$$

Hence q_3 is positive for large ξ if

$$\frac{h^2}{\Delta t} < \frac{2}{\left(\sin(\omega h/2) + \sqrt{1 + \sin^2(\omega h/2)} \right)^2},$$

which is equivalent to

$$\Delta t > \frac{h^2}{2} \left(\sin(\omega h/2) + \sqrt{1 + \sin^2(\omega h/2)} \right)^2 \geq \frac{h^2}{2}. \tag{31}$$

TABLE II
The Largest Stable Time Step Δt_* for Different Grid Sizes

N	h	Δt_*	$\Delta t_*/h^2$
10	0.62832	—	—
20	0.31416	0.355	3.60
40	0.15708	0.053	2.15
80	0.07854	0.011	1.78
160	0.03927	0.0025	1.62
320	0.01963	0.00060	1.56

If $\Delta t > \Delta t_*$, then $q_3(\xi) = 0$ for $0 < \xi < 2/\Delta t$ for at least one ω, which makes the method unstable.

Since there are no poles in q_3 for $\xi > 1/\Delta t$, and q_3 changes sign when the time-step satisfies (31), there must be at least one zero in $q_3(\xi)$ for $\xi > 1/\Delta t$. We summarize these observations in

LEMMA 3.6. *There is at least one zero of $q_3(s)$ in $\Re(s) \geq 0$ if the time-step satisfies* (31).

Note that there are no real-valued zeros of q_3 if $\Delta t \leq h^2/2$. As Δt is increased to satisfy

$$\frac{h^2}{2}\left(\sin(h/2) + \sqrt{1+\sin^2(h/2)}\right) < \Delta t < \frac{h^2}{2}\left(\sin(2h/2) + \sqrt{1+\sin^2(2h/2)}\right),$$

the zero occurs only for $\omega = 1$. Hence, this instability occurs first for the lowest Fourier mode. Naturally, as Δt is increased further, the zero will eventually appear for all ω.

For real-valued s, the unstable region $|\kappa| > 1$ corresponds to $0 < \xi < 2/\Delta t$. Hence, only if the zero of q_3 occurs for $\xi < 2/\Delta t$ does it make the difference method unstable. Since it is hard to solve $q_3(\xi) = 0$ analytically, we did a numerical investigation for various grid sizes. The result is presented in Table II. We note that for fine grids, the time-step restriction in (31) is approximately three times too strict, i.e., the time-step can be three times larger before the method becomes unstable. However, the time-step restriction is similar to that in an explicit scheme, so the lagging of time in the boundary condition $D_0^y p^{n+1} = \frac{2}{h} D_+^y v^n$ ruins the stability of the scheme.

3.3. The Curl–Curl Condition

The lagged velocity in the boundary condition $D_0^y p^{n+1} = -D_0^x D_0^y u^n$ leads to $\kappa D_0^y \hat{p}(0) = -\frac{i}{h}\sin(\omega h) D_0^y \hat{u}(0)$. Therefore, the equation for P becomes

$$P\left(\frac{\kappa \sinh(\alpha h)}{h} - \frac{\sin^2(\omega h)}{h^2 s}\left(\frac{\sinh(\beta h)}{h} - \frac{\sinh(\alpha h)}{h}\right)\right) = 0,$$

which is equivalent to

$$P\left(\frac{\sinh(\alpha h)}{h(1-s\Delta t)} - \frac{\sin^2(\omega h)}{h^2 s}\left(\frac{\sinh(\beta h)}{h} - \frac{\sinh(\alpha h)}{h}\right)\right) = 0. \tag{32}$$

As before, there are nontrivial solutions for $\omega = 0$ that correspond to the undetermined constant in the pressure. This mode is removed by enforcing the mean of the pressure to be

zero. For $\omega > 0$ we consider

$$q_4(s) = \frac{h^2 \sinh(\alpha h)}{1 - s\Delta t} - \sin^2(\omega h) q(s).$$

We have

$$\Im(q_4(s)) = \Im(s) \frac{h^2 \Delta t \sinh(\alpha h)}{|1 - s\Delta t|^2} - \sin^2(\omega h) \Im(q(s)).$$

For $\Im(s) > 0$, the first term is positive, and by Lemma 2.3, so is the second term. Conversely, for $\Im(s) < 0$, both terms are negative. We have proven

LEMMA 3.7. *The function $q_4(s)$ satisfies $\Im(q_4(s)) = 0$ if and only if $\Im(s) = 0$.*

We proceed by studying $q_4(s)$ for real-valued $s = \xi$, $\Im(\xi) = 0$. We begin with the case $0 \le \xi < 1/\Delta t$. From (24) and the properties of the function q_2, we get

$$q_4(\xi) \ge q_2(\xi) > 0, \quad 0 \le \xi < \frac{1}{\Delta t}.$$

The second case is $\xi > 1/\Delta t$. Now both terms in q_4 are negative, so

$$q_4(\xi) < 0, \quad \xi > \frac{1}{\Delta t}.$$

At $\xi = 1/\Delta t$, q_4 becomes unbounded, so we conclude that $q_4(\xi) \neq 0$ for $\xi \ge 0$. We present an example of $q_4(\xi)$ in Fig. 4. To summarize, there are no nontrivial solutions of (32) for $\Re(s) \ge 0$. Hence, there are no eigenvalues of (27) with $|\kappa| \ge 1$ for $\Delta t > 0$ when the boundary condition $D_0^y \kappa \hat{p}(\omega, 0, \kappa) = -\frac{i}{h} \sin(\omega h) D_0^y \hat{u}(\omega, 0, \kappa)$ is used.

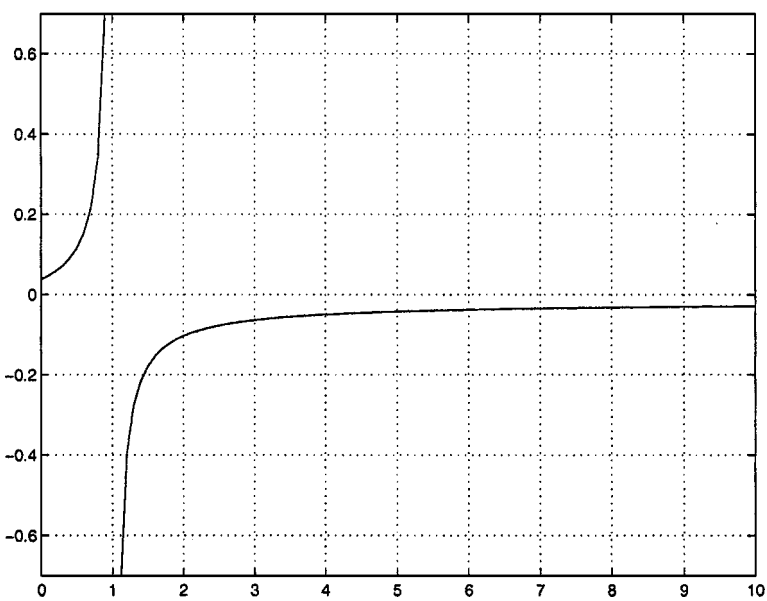

FIG. 4. The function $q_4(\xi)$ for real-valued ξ for the case $n = 15$, $\omega = 1$, and $\Delta t = 1$. Note that there is a pole at $\xi = 1$, where q_4 becomes unbounded.

4. NUMERICAL COMPUTATION OF AMPLIFICATION FACTORS

In this section we numerically compute the amplification factors for Stokes equations discretized by backward Euler in time, and for a semi-implicit discretization of the linearized Navier-Stokes equations where the viscous term is treated implicitly and the convective term is handled explicitly.

We consider a rectangular domain Ω: $0 \le x \le 2\pi$, $0 \le y \le 1$, where the solution is 2π-periodic in the x-direction, with no-slip boundary conditions at $y = 0$ and $y = 1$. The computational grid is given by $x_j = (j-1)\Delta x$, $\Delta x = 2\pi/N$, $1 \le j \le N$, and $y_k = (k-1)\Delta y$, $\Delta y = 1/(M-1)$, $0 \le k \le M+1$. The extra grid lines $k = 0$ and $k = M+1$ outside the no-slip boundaries are used to help discretize the boundary conditions. Since the boundary conditions are the same for both Stokes and the linearized Navier–Stokes equations, we begin by discussing them. Here, the boundary conditions will be used for solving an eigenvalue problem corresponding to (27), so they will be expressed in the transformed variables $(\hat{\boldsymbol{u}}, \hat{p})$.

We apply the momentum equations at all interior points $2 \le k \le M-1$ and the no-slip boundary conditions at $k = 1$ and $k = M$. The pressure equation will be applied at all interior points and on the boundaries: $1 \le k \le M$. Hence, to get the same number of equations as unknowns, we will need three additional equations at each boundary. We will use the following conditions at the $y = 0$ boundary. Corresponding relations are imposed at the $y = 1$ boundary.

1. The coupled condition. Together with the zero divergence condition, enforce the v-momentum equation and extrapolate u:

$$\begin{cases} (D_+^y)^4 \hat{u}_{j,0} = 0, \\ D_0^y \hat{v}_{j,1} = 0, \\ D_0^y \kappa \hat{p}_{j,1} = D_+^y D_-^y \kappa \hat{v}_{j,1}. \end{cases} \tag{33}$$

Note that the value of $\hat{u}$ on the ghost point is not used by any other equation.

2. The div–grad condition:

$$\begin{cases} (D_+^y)^4 \hat{u}_{j,0} = 0, \\ D_0^y \hat{v}_{j,1} = 0, \\ D_0^y \kappa \hat{p}_{j,1} = D_+^y D_-^y \hat{v}_{j,1}. \end{cases} \tag{34}$$

Note that the only difference compared to the coupled condition is the absence of the factor κ on the right-hand side of the last equation.

3. The curl–curl condition:

$$\begin{cases} (D_+^y)^4 \hat{u}_{j,0} = 0, \\ (D_+^y)^4 \hat{v}_{j,0} = 0, \\ D_0^y \kappa \hat{p}_{j,1} = -\frac{i}{h} \sin(\omega h) D_0^y \hat{u}_{j,1}. \end{cases} \tag{35}$$

Note that the value of $\hat{v}$ on the ghost point is not used by any other equation.

4.1. Implicit Discretization of Stokes Equations

We consider the eigenvalue problem (27) from Section 3, but now in the periodic channel domain with one of the boundary conditions (33), (34), or (35). For computational convenience, we introduce the new variable $\hat{q} = \kappa\hat{p}$ and solve for $(\hat{u}, \hat{v}, \hat{q})$. By setting $\lambda = (\kappa - 1)/\Delta t$, we get the generalized eigenvalue problem

$$\begin{aligned}
\lambda\hat{u} - \lambda\Delta t L_h\hat{u} &= -\frac{i}{\Delta x}\sin(\omega\Delta x)\hat{q} + L_h\hat{u}, && 2 \le k \le M-1,\\
\lambda\hat{v} - \lambda\Delta t L_h\hat{v} &= -D_0^y\hat{q} + L_h\hat{v}, && 2 \le k \le M-1,\\
L_h\hat{q} &= 0, && 1 \le k \le M,\\
\hat{\boldsymbol{u}}_{j,k} &= 0, && k = 1, M,
\end{aligned}$$

where L_h is the discretized, Fourier-transformed, Laplace operator:

$$L_h\hat{u} = -\frac{4}{\Delta x^2}\sin^2(\omega\Delta x/2)\hat{u} + D_+^y D_-^y\hat{u}.$$

In addition, the eigenfunctions are subject to one of the boundary conditions (33), (34), or (35). In matrix form, the eigenvalue problem can be written

$$A\boldsymbol{x} = \lambda B\boldsymbol{x}, \quad \boldsymbol{x} = (\hat{u}_0, \ldots, \hat{u}_{M+1}, \hat{v}_0, \ldots, \hat{v}_{M+1}, \hat{q}_0, \ldots, \hat{q}_{M+1})^T.$$

We show an example of the structure of the nonzero elements in A and B in Fig. 5.

We solve the generalized eigenvalue problem for $1 \le \omega \le N-1$ by using the QZ-algorithm in Matlab (for $\omega = 0$, the problem becomes singular due to the undetermined constant in the pressure). The amplification factors $\kappa = 1 + \lambda\Delta t$ when the coupled condition (33) is used are shown in Fig. 6. The case when the div–grad condition (34) is applied is presented in Fig. 7. Finally, the case when the curl–curl condition (35) is used is displayed in Fig. 8.

In agreement with the analysis in Section 3, these computations indicate that the div–grad condition (34) leads to an unstable discretization (for this time-step), while the coupled condition (33) and the curl–curl condition (35) both lead to stable discretizations.

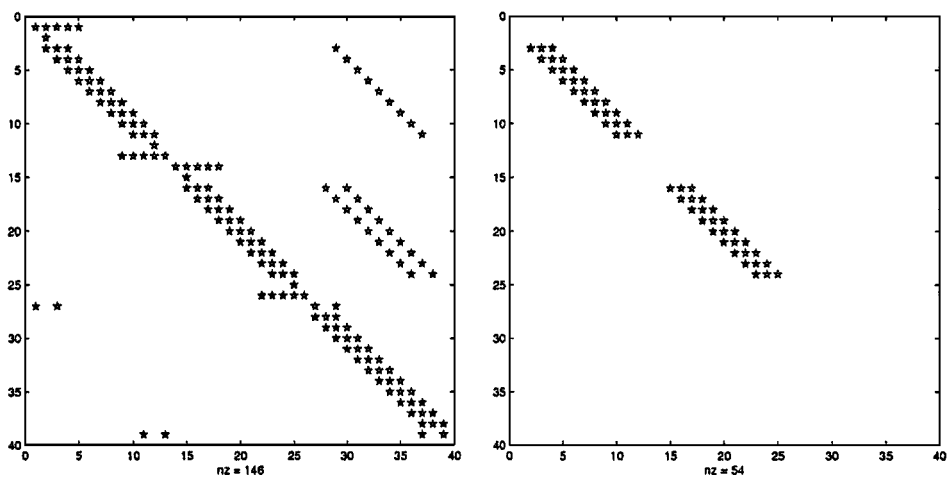

FIG. 5. The structure of the nonzero elements in the matrices A (left) and B (right) for the curl–curl condition, $M = 11$, $N = 10$, and $\omega = 5$.

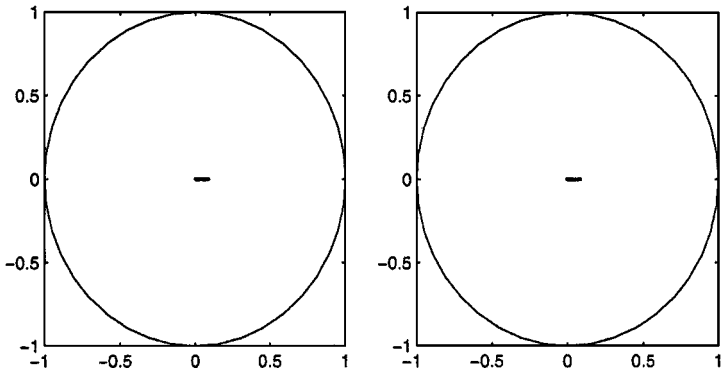

FIG. 6. The amplification factors κ for the coupled condition (33) for the case $\Delta t = 1$ and $N = 10$, $M = 11$ (left), and $N = 20$, $M = 21$ (right). Note that both cases are stable. The solid line represents the neutral stability curve $|\kappa| = 1$.

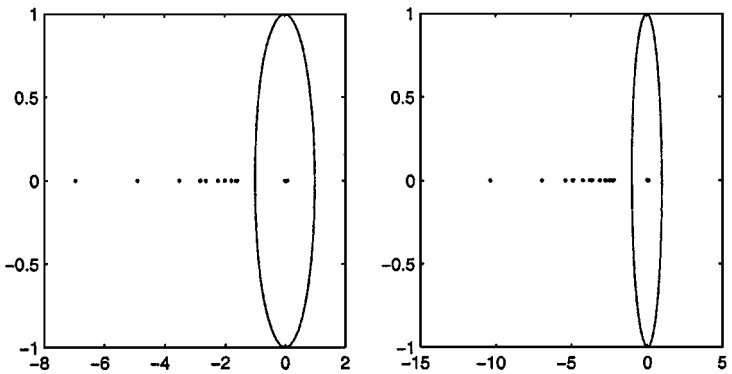

FIG. 7. The amplification factors κ for the div–grad condition (34) for the case $\Delta t = 1$ and $N = 10$, $M = 11$ (left), and $N = 20$, $M = 21$ (right). Note that both cases are unstable, and the instability gets worse as the grid is refined. The solid line represents the neutral stability curve $|\kappa| = 1$.

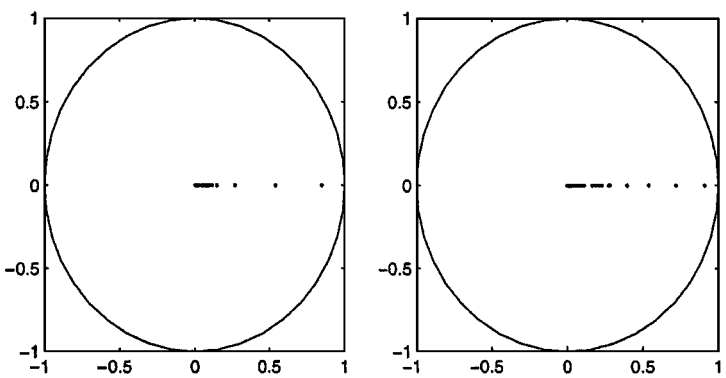

FIG. 8. The amplification factors κ for the curl–curl condition (35) for the case $\Delta t = 1$ and $N = 10$, $M = 11$ (left), and $N = 20$, $M = 21$ (right). Note that both cases are stable. The solid line represents the neutral stability curve $|\kappa| = 1$.

4.2. Viscous-Implicit Discretization of Navier–Stokes Equations

To analyze the stability of the incompressible Navier–Stokes equations (1), we start by linearizing the problem around smooth velocity and pressure fields;

$$p = P + \epsilon p', \quad \boldsymbol{u} = \boldsymbol{U} + \epsilon \boldsymbol{u}', \quad \boldsymbol{U} = \begin{pmatrix} U \\ V \end{pmatrix}, \quad \boldsymbol{u}' = \begin{pmatrix} u' \\ v' \end{pmatrix},$$

where $0 < \epsilon \ll 1$. After skipping the prime and setting the forcing to zero, the linearized equations read

$$\begin{aligned} \boldsymbol{u}_t + (\boldsymbol{u} \cdot \nabla)\boldsymbol{U} + (\boldsymbol{U} \cdot \nabla)\boldsymbol{u} + \nabla p &= \nu \nabla^2 \boldsymbol{u}, \\ \nabla^2 p + 2U_x u_x + 2U_y v_x + 2V_x u_y + 2V_y v_y &= 0. \end{aligned} \tag{36}$$

As in the previous sections, we discretize (36) by second-order accurate centered differences in space. Time is discretized by a mixed forward Euler/backward Euler scheme, where the viscous term is treated implicitly and the convective term is handled explicitly.

To analyze the stability of the scheme, the variable coefficients are frozen and the problem is Fourier transformed in the x-direction, resulting in

$$\frac{\hat{\boldsymbol{u}}^{n+1} - \hat{\boldsymbol{u}}^n}{\Delta t} + A_E(\boldsymbol{U})\hat{\boldsymbol{u}}^n + G_h \hat{p}^{n+1} = \nu L_h \hat{\boldsymbol{u}}^{n+1},$$

where G_h is the discretized, Fourier-transformed gradient operator

$$G_h \hat{p} = \begin{pmatrix} \frac{i \sin(\omega \Delta x)}{\Delta x} \\ D_0^y \end{pmatrix} \hat{p},$$

and $A_E(\boldsymbol{U})$ corresponds to the linearized convective term

$$A_E(\boldsymbol{U})\hat{\boldsymbol{u}} = \left(D_0^x \boldsymbol{U}\right)\hat{u} + U \frac{i \sin(\omega \Delta x)}{\Delta x}\hat{\boldsymbol{u}} + \left(D_0^y \boldsymbol{U}\right)\hat{v} + V D_0^y \hat{\boldsymbol{u}}.$$

After discretization and Fourier transformation, the linearized pressure equation in (36) becomes

$$L_h \hat{p}^{n+1} = R_h(\boldsymbol{U})\hat{\boldsymbol{u}}^n, \tag{37}$$

where

$$\begin{aligned} R_h(\boldsymbol{U})\hat{\boldsymbol{u}}^n = &-2\left(D_0^x V\right) D_0^y \hat{u}^n - 2\left(D_0^y V\right) D_0^y \hat{v}^n - 2\left(D_0^x U\right) \frac{i \sin(\omega \Delta x)}{\Delta x}\hat{u}^n \\ &- 2\left(D_0^y U\right) \frac{i \sin(\omega \Delta x)}{\Delta x}\hat{v}^n. \end{aligned}$$

To derive the eigenvalue problem, we make the ansatz (26), and set $\hat{q} = \kappa \hat{p}$ and $\kappa = 1 + \lambda \Delta t$. This yields

$$\begin{aligned} \lambda \hat{\boldsymbol{u}} - \lambda \Delta t \nu L_h \hat{\boldsymbol{u}} &= -A_E(\boldsymbol{U})\hat{\boldsymbol{u}} - G_h \hat{q} + \nu L_h \hat{\boldsymbol{u}}, && 2 \le k \le M-1, \\ L_h \hat{q} &= R_h(\boldsymbol{U})\hat{\boldsymbol{u}}, && 1 \le k \le M, \\ \hat{\boldsymbol{u}}_{j,k} &= 0, && k = 1, M. \end{aligned} \tag{38}$$

In addition, the eigenfunctions are subject to one of the pressure boundary conditions (33), (34), or (35).

We linearize the equations around the divergence-free velocity field

$$\begin{pmatrix} U(x,y) \\ V(x,y) \end{pmatrix} = \begin{pmatrix} \sin^2(\pi x/4)\sin(\pi y/2) \\ -\sin(\pi x/2)\sin^2(\pi y/4) \end{pmatrix}, \tag{39}$$

where the coefficients are frozen at $x = 0.5$.

In order to estimate the largest stable time-step, we proceed by performing a von Neumann analysis of the spectrum. For this purpose, we neglect the boundaries at $y = 0$ and $y = 1$, assume that the solution is 2π-periodic in both x and y, and Fourier transform the problem in both directions. For simplicity, we neglect all zeroth-order terms, and we disregard the pressure. Then the u- and v-equations decouple and we get the approximate expression for the amplification factor,

$$\frac{\kappa_a - 1}{\Delta t} + ia = -\nu\kappa_a b,$$

where

$$a(\omega,\omega_2) = U\frac{\sin(\omega\Delta x)}{\Delta x} + V\frac{\sin(\omega_2\Delta y)}{\Delta y},$$
$$b(\omega,\omega_2) = \frac{4}{\Delta x^2}\sin^2(\omega\Delta x/2) + \frac{4}{\Delta y^2}\sin^2(\omega_2\Delta y/2).$$

We have

$$\kappa_a = \frac{1 - ia\Delta t}{1 + \nu b\Delta t}.$$

Since $|a| > 0$ for $\omega > 0$ or $\omega_2 > 0$, we see that $|\kappa_a| > 1$ if $\nu = 0$. Hence, the scheme is unstable for all Δt when $\nu = 0$. However, for $\nu > 0$, the factor b improves the situation since $b > 0$ for $\omega > 0$ and $\omega_2 > 0$. In this case the scheme is stable for sufficiently small Δt. Given $\boldsymbol{U}$, ν, and the grid sizes, the largest Δt that satisfies $|\kappa_a| \le 1$ for all $0 \le \omega \le N - 1$ and $0 \le \omega_2 \le M - 1$ can be computed numerically. For the case $\nu = 0.05$, $N = 10$ ($\Delta x = \pi/5$) and $M = 11$ ($\Delta y = 1/10$), we get $\Delta t \approx 1.44$. This time-step also makes $|\kappa_a| < 1$ for $M = 21$ and $N = 20$.

We solve the eigenvalue problem (38) for the three different pressure boundary conditions by using Matlab. In Figs. 9, 10, and 11, we show the corresponding amplification factors. In these computations, we used $\Delta t = 1.44$ and $\nu = 0.05$. Similar to the implicit discretization of Stokes equation, the div–grad condition leads to an unstable scheme, while the curl– curl condition gives a stable scheme. The coupled condition has one pair of eigenvalues with $|\kappa| > 1$ for the finer grid, but stability was regained when the time-step was reduced to $\Delta t = 1$.

After some experimentation, we found that the case with the div–grad condition could be made stable by decreasing the time-step to $\Delta t \approx 0.073$ (for $N = 20$, $M = 21$), which is almost 20 times smaller than the original time-step. Also note that $\Delta y^2/\nu = 0.05$, so the stable time-step is approximately $1.46\Delta y^2/\nu$, which agrees well with the analysis in Section 3.2.

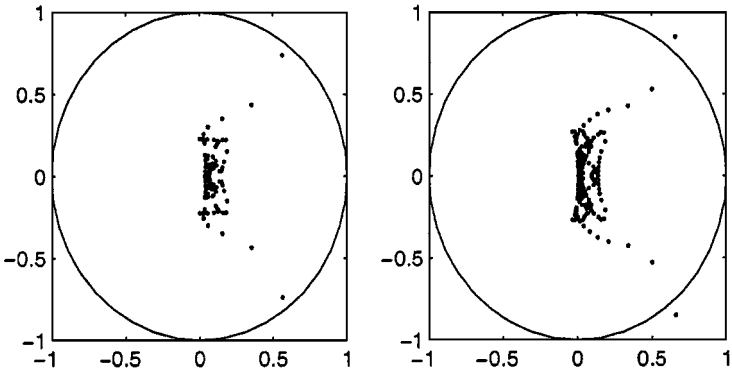

FIG. 9. The amplification factors κ for the viscous-implicit treatment of the Navier–Stokes equations with the coupled condition (33) for the case $\Delta t = 1.44$, $\nu = 0.05$. The resolution is $N = 10$, $M = 11$ (left), and $N = 20$, $M = 21$ (right). Note that the fine grid has two unstable eigenvalues for this time-step. The solid line represents the neutral stability curve $|\kappa| = 1$.

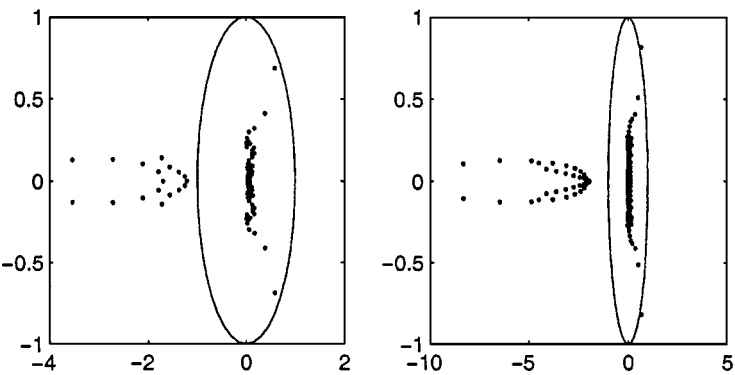

FIG. 10. The amplification factors κ for the viscous-implicit treatment of the Navier–Stokes equations with the div–grad condition (34) for the case $\Delta t = 1.44$, $\nu = 0.05$. The resolution is $N = 10$, $M = 11$ (left), and $N = 20$, $M = 21$ (right). Note that both cases are unstable and that the instability gets worse as the grid is refined. The solid line represents the neutral stability curve $|\kappa| = 1$.

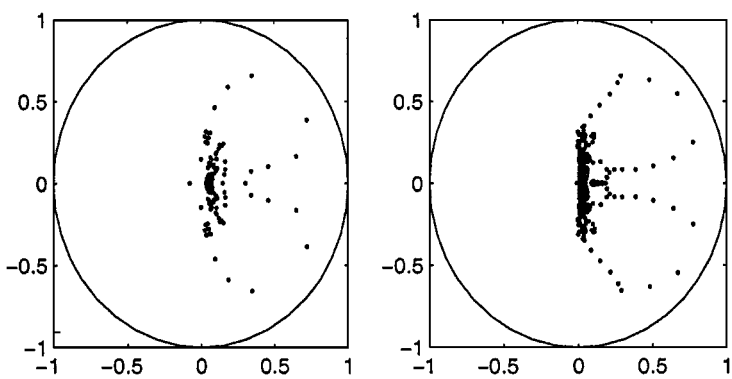

FIG. 11. The amplification factors κ for the viscous-implicit treatment of the Navier–Stokes equations with the curl–curl condition (35) for the case $\Delta t = 1.44$, $\nu = 0.05$. The resolution is $N = 10$, $M = 11$ (left), and $N = 20$, $M = 21$ (right). Note that both cases are stable. The solid line represents the neutral stability curve $|\kappa| = 1$.

5. FLOW AROUND CYLINDERS

In this section, we numerically solve the incompressible Navier–Stokes equations to test both split pressure boundary conditions as well as the inaccurate, but commonly used [9, 10], homogeneous Neumann condition

$$\frac{\partial p}{\partial n} = 0, \quad (x, y) \in \partial\Omega. \tag{40}$$

We solve the equations by using the OverBlown solver [6], which is based on the Overture class library. OverBlown uses overlapping (Chimera) grids to discretize the unsteady incompressible Navier–Stokes equations in velocity-pressure formulation. For this reason, we cannot use it to test the coupled condition, which would require a simultaneous solution of the momentum and pressure equations.

While the solver is capable of simulating both 2-D and 3-D problems in rather complicated geometries, we use it to demonstrate the stability characteristics of the pressure boundary conditions. For this purpose we find it sufficient to study unsteady 2-D flow past circular cylinders in a channel.

To make the time-integration efficient, we only use the semi-implicit technique on component grids where the viscous term dominates the convective term. Often, this is the case for components with a no-slip boundary, where the grid needs to be fine in order to resolve boundary layers. On the other components, we employ an explicit method.

The semi-implicit technique consists of a second-order Adams–Bashforth/Adams–Moulton predictor–corrector scheme for the convective part coupled to a second-order Crank–Nicholson scheme for the viscous part. To describe the scheme, we split the incompressible Navier–Stokes equations (1) according to

$$\boldsymbol{u}_t = L_1\boldsymbol{u} + L_2\boldsymbol{u} + \boldsymbol{f},$$

where

$$\begin{aligned} L_1\boldsymbol{u} &= -(\boldsymbol{u}\cdot\nabla)\boldsymbol{u} - \nabla p, \\ L_2\boldsymbol{u} &= \nu\nabla^2\boldsymbol{u}, \end{aligned}$$

and p satisfies the pressure equation in (1). Then each time-step consists of a predictor

$$\frac{\boldsymbol{u}^p - \boldsymbol{u}^n}{\Delta t} = \frac{3}{2}L_1\boldsymbol{u}^n - \frac{1}{2}L_1\boldsymbol{u}^{n-1} + \frac{1}{2}(L_2\boldsymbol{u}^p + L_2\boldsymbol{u}^n) + \frac{3}{2}\boldsymbol{f}^n - \frac{1}{2}\boldsymbol{f}^{n-1},$$

followed by a corrector

$$\frac{\boldsymbol{u}^{n+1} - \boldsymbol{u}^n}{\Delta t} = \frac{1}{2}L_1\boldsymbol{u}^p + \frac{1}{2}L_1\boldsymbol{u}^n + \frac{1}{2}(L_2\boldsymbol{u}^{n+1} + L_2\boldsymbol{u}^n) + \frac{1}{2}\boldsymbol{f}^{n+1} + \frac{1}{2}\boldsymbol{f}^n.$$

Note that the scheme is explicit in the pressure. For example, let us denote the pressure occurring in $L_1\boldsymbol{u}^n$ by p^n. It is computed by solving

$$\nabla^2 p^n + \nabla u^n \cdot \boldsymbol{u}_x^n + \nabla v^n \cdot \boldsymbol{u}_y^n = \nabla\cdot\boldsymbol{f},$$

together with one of the pressure boundary conditions.

The explicit time-integration method, which is used on component grids where the convective term dominates the viscous term, is obtained by applying the Adams–Bashforth/Adams–Moulton predictor–corrector scheme to both the convective and the viscous terms.

Due to truncation errors and because of the interpolation between components in the overlapping grid, the divergence will not be identically zero in the numerical computation. To suppress the spurious divergence, an extra term is added to the pressure equation in the OverBlown solver:

$$\nabla^2 p + \nabla u \cdot \boldsymbol{u}_x + \nabla v \cdot \boldsymbol{u}_y = \nabla \cdot \boldsymbol{f} + C(\boldsymbol{x}) \nabla \cdot \boldsymbol{u}.$$

This term can be viewed as a divergence sink, since it appears as a sink in the equation for the divergence. The OverBlown documentation [6] provides a detailed description of the coefficient $C(\boldsymbol{x})$.

We start by checking the accuracy and stability of the solver by applying the method of an exact solution: see Chesshire and Henshaw [2]. We choose the exact solution to be

$$\begin{aligned} u_e(x, y, t) &= \frac{1}{2} \cos(\pi x/2) \cos(\pi y/2) \cos(\pi t/2) + \frac{1}{2}, \\ v_e(x, y, t) &= \frac{1}{2} \sin(\pi x/2) \sin(\pi y/2) \cos(\pi t/2) + \frac{1}{2}, \\ p_e(x, y, t) &= \cos(\pi x/2) \cos(\pi y/2) \cos(\pi t/2) + \frac{1}{2}. \end{aligned} \tag{41}$$

The forcing is constructed by inserting the exact solution (41) into (1). For example, the u-component of the momentum equation yields

$$f^{(u)} =: \frac{\partial u_e}{\partial t} + \boldsymbol{u}_e \cdot \nabla u_e + \frac{\partial p_e}{\partial x} - \nu \nabla^2 u_e.$$

The forced problem is solved numerically and the truncation error can be computed by taking the difference between the exact and the numerical solution. Furthermore, the order of accuracy can be estimated by refining the grid. Note that only one level of refinement is necessary, since the truncation error can be computed exactly. In the computations, the initial data is $\boldsymbol{u}_0(x, y) = \boldsymbol{u}_e(x, y, 0)$, $\nu = 0.01$, and the truncation error was evaluated at time $t = 1$. The computational grid is shown in Fig. 12 and the results are presented in Table III. Note that all three boundary conditions yield second-order accurate velocities and divergence. The apparent superconvergence of the pressure is caused by the divergence sink in the pressure equation.

The time-step used for the curl–curl condition and the simplified Neumann condition was calculated by a von Neumann analysis based on only the convective part of the equations. The computations indicate that the scheme is stable for this time-step. However, for the div–grad condition, the time-step needs to be much smaller. The time-steps reported in Table III are the largest values that gave a stable scheme. Also note that in this case, the time-step is proportional to the square of the grid size, instead of being proportional to the grid size itself, as it is when the curl–curl condition is applied.

The simplified Neumann condition (40) is apparently stable for the same time-step as the curl–curl condition. In this forced computation, a forcing is also added to the boundary conditions, which makes the simplified Neumann condition compatible with the momentum

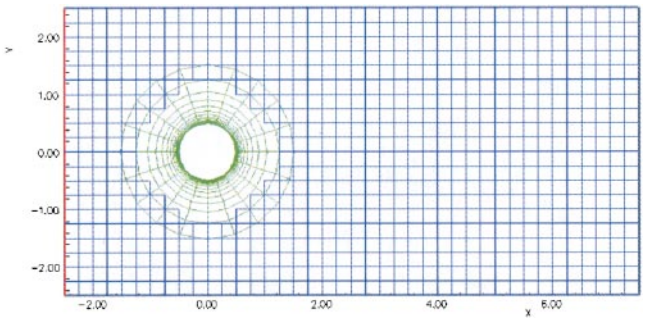

FIG. 12. The coarser of the grids used in the convergence study with 41×21 points in the rectangular grid and 21×14 points in the circular grid. The finer counterpart of this grid had $81 \times 41 \cup 41 \times 27$ points. A no-slip boundary condition was imposed on the circle, and slip conditions were used on the horizontal boundaries of the rectangle. The left boundary had a prescribed velocity condition (inflow) and an outflow condition was prescribed on the right boundary.

equations. Therefore, the divergence remains small in these computations. However, in the unforced case, the simplified Neumann condition is not compatible with the momentum equations, so it cannot be expected to perform as well.

We proceed by studying the unsteady flow around two cylinders in a rectangular channel to evaluate the curl–curl condition and the simplified homogeneous Neumann condition (40). The channel has the dimensions $[-2.5, 7.5] \times [-2.5, 2.5]$ with slip boundaries on the horizontal sides, prescribed velocity on the left (inflow) boundary, and an outflow condition on the right boundary. Both cylinders have radius 0.5 and they are centered at $\boldsymbol{x} = (0, 0.75)$ and $\boldsymbol{x} = (0.5, -0.75)$. To conserve computational resources, we construct a grid with several components to concentrate grid points in the regions where the solution can be expected to vary rapidly; see Fig. 13. We start the computation from rest, $\boldsymbol{u}_0(x, y) = 0$, and accelerate the flow smoothly up to time $t = 1$ by prescribing the horizontal velocity component on the inflow boundary to be

$$U_{in}(t) = \begin{cases} 0, & t \le 0, \\ 3t^2 - 2t^3, & 0 < t \le 1, \\ 1, & t > 1. \end{cases} \tag{42}$$

Shortly after the acceleration of the fluid is completed, the flow develops an oscillating

TABLE III
Truncation Errors for the Forced Computation for the Div–Grad and Curl–Curl Conditions as Well as the Simplified Homogeneous Neumann Condition

BC	Grid	Δt	$\|p - p_e\|_\infty$	$\|u - u_e\|_\infty$	$\|v - v_e\|_\infty$	$\|\nabla \cdot \boldsymbol{u}\|_\infty$
div–grad	coarse	$2.0 \cdot 10^{-3}$	$5.8 \cdot 10^{-2}$	$4.2 \cdot 10^{-2}$	$8.6 \cdot 10^{-2}$	$1.1 \cdot 10^{-1}$
div–grad	fine	$5.0 \cdot 10^{-4}$	$5.7 \cdot 10^{-3}$	$8.8 \cdot 10^{-3}$	$1.5 \cdot 10^{-2}$	$2.4 \cdot 10^{-2}$
curl-curl	coarse	$1.1 \cdot 10^{-2}$	$5.8 \cdot 10^{-2}$	$4.2 \cdot 10^{-2}$	$8.6 \cdot 10^{-2}$	$1.1 \cdot 10^{-1}$
curl–curl	fine	$5.5 \cdot 10^{-3}$	$5.8 \cdot 10^{-3}$	$8.8 \cdot 10^{-3}$	$1.5 \cdot 10^{-2}$	$2.4 \cdot 10^{-2}$
simple	coarse	$1.1 \cdot 10^{-2}$	$7.3 \cdot 10^{-2}$	$4.2 \cdot 10^{-2}$	$8.6 \cdot 10^{-2}$	$1.2 \cdot 10^{-1}$
simple	fine	$5.5 \cdot 10^{-3}$	$9.1 \cdot 10^{-3}$	$8.8 \cdot 10^{-3}$	$1.5 \cdot 10^{-2}$	$2.4 \cdot 10^{-2}$

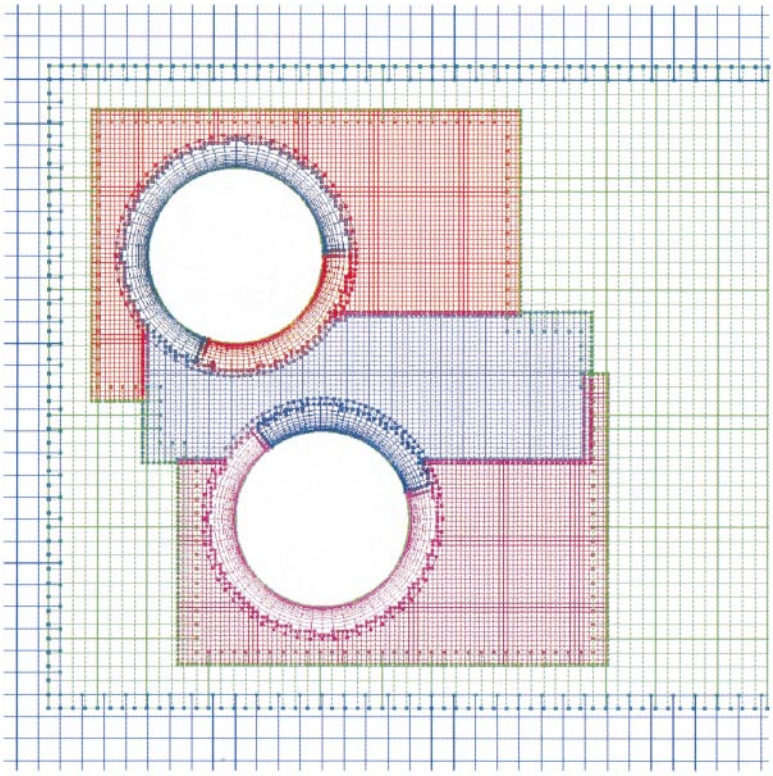

FIG. 13. A closeup of the grid used to compute the flow around two cylinders. This grid has 9 components with a total of 26,223 grid points, of which 14,256 are discretization points, 10,017 are (unused) hole points and 1,950 are interpolation points. The semi-implicit time-integration method was used on the component grids with a boundary on one of the circles, and the explicit method was used on all Cartesian grids.

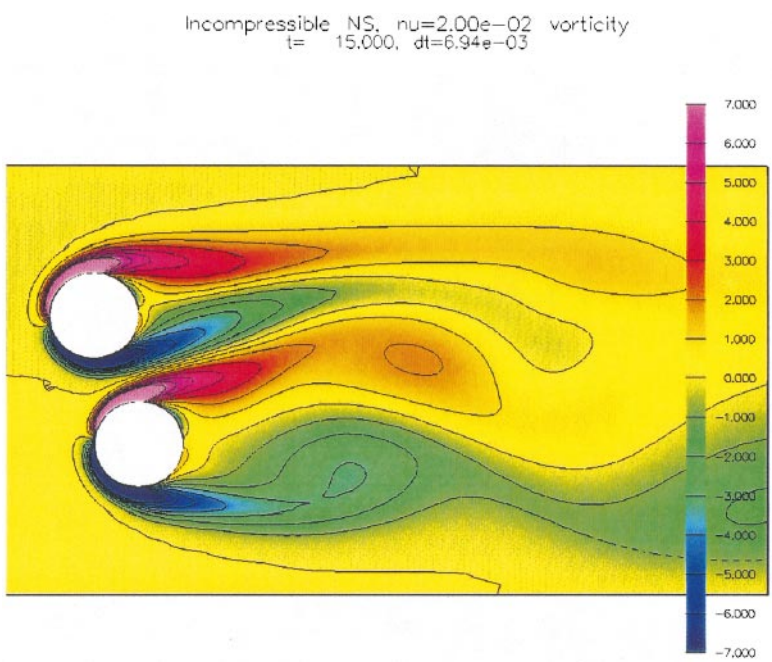

FIG. 14. The vorticity around the two cylinders at time $t = 15$.

pattern where the von Karman vortices behind the two cylinders interact. In the present computation, the viscosity was $\nu = 0.02$, which corresponds to a Reynolds number of 50 based on the diameter of a cylinder. As an example, we show the vorticity at time $t = 15$ in Fig. 14. An interesting observation is that essentially the same solution is obtained when the homogeneous Neumann condition (40) is used. However, close to the no-slip walls on the cylinders, a divergence boundary layer is formed. The net effect of the divergence is to change the shape of the cylinders such that they become slightly more streamlined; see Fig. 15. When the homogeneous Neumann condition is used, the divergence in the boundary layer is negative on the upstream side and positive on the upper and lower sides. As a consequence, streamlines enter through the cylinder on its upstream side and exit on the upper and the lower sides of the cylinder, which makes the curvature of the streamlines

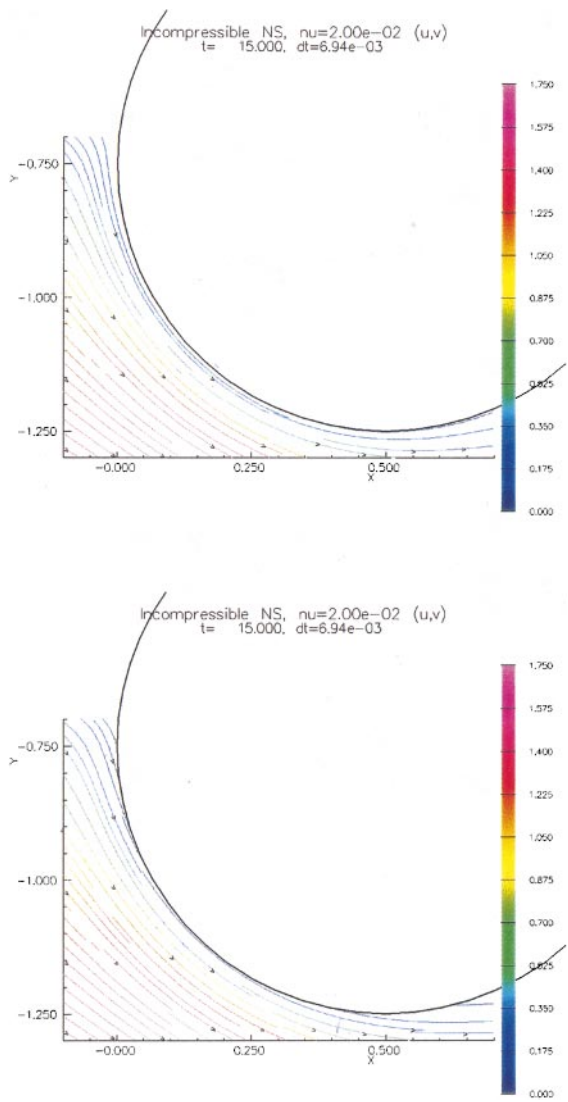

FIG. 15. Streamlines around parts of the lower cylinder for the curl–curl condition (top) and the homogeneous Neumann condition (bottom).

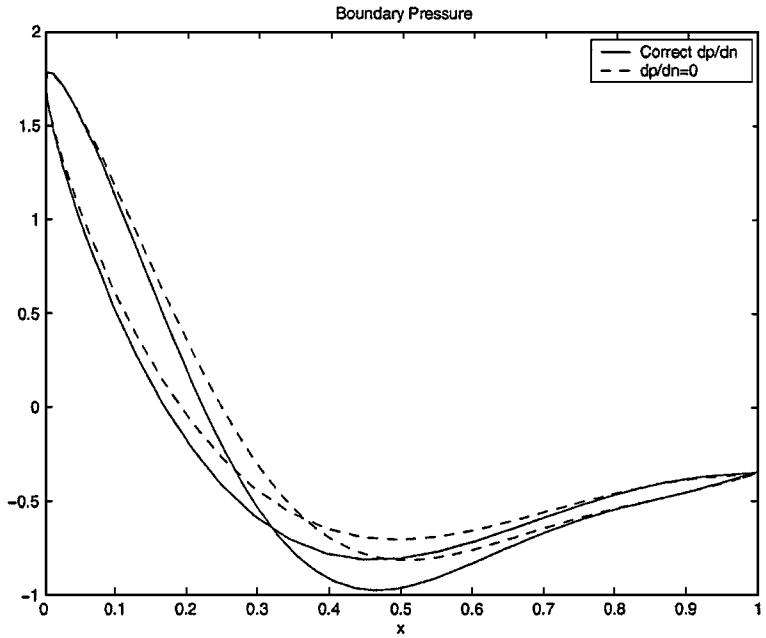

FIG. 16. The pressure as a function of x on the lower cylinder.

smaller. It can therefore be expected that the pressure on the cylinder is affected; see Fig. 16. Furthermore, integrated quantities such as lift, drag, and torque are also affected adversely by the simplified pressure boundary condition; see Table IV. We conclude that the use of the homogeneous Neumann boundary condition for the pressure gives questionable results, especially close to no-slip boundaries.

As a final experiment, we study how the curl–curl boundary condition performs at a higher Reynolds number, where boundary layers get thinner and the normal derivative of the pressure becomes smaller. The normal derivative of the divergence is forced to be zero on no-slip boundaries by the balance between the viscous terms in the momentum equations and in the curl–curl boundary condition. Subtracting (7) from the normal component of the momentum equations in (1) applied to a no-slip boundary yields

$$0 = \nu \boldsymbol{n} \cdot (\nabla^2 \boldsymbol{u} + \nabla \times \nabla \times \boldsymbol{u}) \equiv \nu \frac{\partial (\nabla \cdot \boldsymbol{u})}{\partial n}. \tag{43}$$

In the discrete case, the momentum equations are only applied in the interior of the domain,

TABLE IV

Forces and Torque About the Point (0.25, 0) on Both Cylinders at Time $t = 15$ when the Curl–Curl Condition and the Simple Homogeneous Neumann Condition Are Used

BC	Drag	Lift	Torque
curl–curl	3.90	0.52	0.41
simple	3.97	0.50	0.38

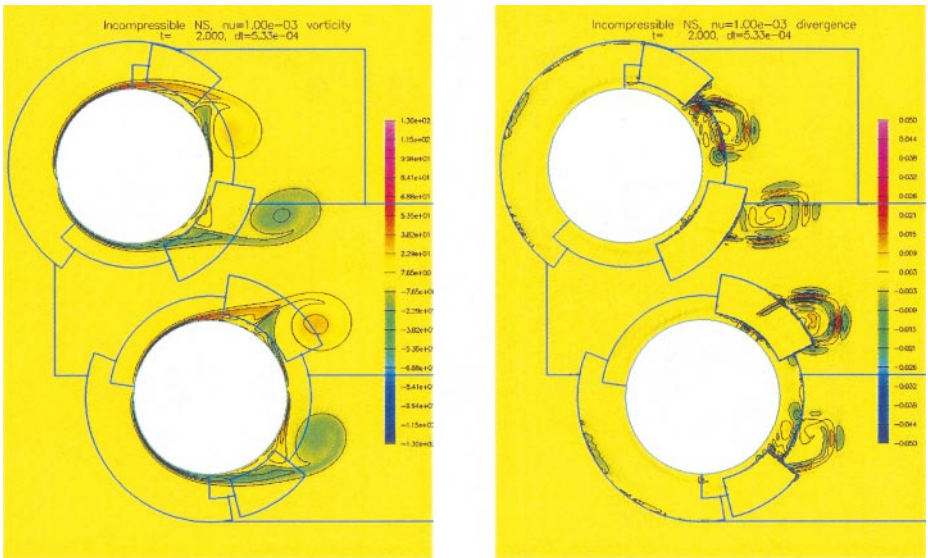

FIG. 17. The vorticity (left) and the divergence (right) at time $t = 2.0$ for the case $\nu = 10^{-3}$. Both the vorticity and the divergence are plotted with 18 equally spaced contour lines. The contour lines are between ± 130 for the vorticity and between ± 0.05 for the divergence. The thick lines show component grid boundaries.

and not on the boundary, so the balance in (43) is perturbed by truncation error terms. Hence, it is interesting to see how the divergence in the numerical solution behaves near the boundary when ν becomes small. For this purpose, we compute the unsteady flow around the two cylinders when $\nu = 10^{-3}$, which corresponds to a Reynolds number of 10^3. Similar to the previous computation, the inflow velocity is smoothly accelerated from rest according to (42). To resolve the solution at this Reynolds number, the resolution was increased to 245,281 grid points, of which 236,355 were discretization points and 8,926 were interpolation points. In Fig. 17, we present the vorticity and the divergence at time $t = 2$. The scheme used in the OverBlown solver is not conservative, so the divergence can only be expected to be small, that is, of the order of the truncation error. We view the amount of divergence as a measure of the accuracy of the velocity gradients in the flow field. Since the divergence is more than two orders of magnitude smaller than the vorticity, we deduce that the solution is adequately resolved on the grid. Furthermore, the divergence is small near all no-slip boundaries and we conclude that the curl–curl boundary condition works well also when ν becomes small.

6. CONCLUSIONS

The stability properties of three different pressure boundary conditions for no-slip walls have been studied in detail. First, we used a normal-mode technique to analyze Stokes equations discretized by centered differences in space and by backward Euler in time on a half-plane problem with only one no-slip boundary. We have proven that the div–grad condition is unstable for time-steps $\Delta t > Ch^2$, where h is the grid size and C is a constant. For the curl–curl condition and the coupled condition, we have shown that the necessary Godunov–Ryabenkii stability condition is satisfied for all $\Delta t > 0$.

For a periodic channel domain with two no-slip boundaries, we have performed numerical computations of the amplification factors. For the Stokes equation, we confirmed the analytical results for the backward Euler scheme. A mixed forward Euler/backward Euler discretization of the linearized Navier–Stokes equations was also studied. Here, the convective term is treated explicitly while the viscous term is handled implicitly. In this case, we have demonstrated that the curl–curl condition and the coupled condition lead to stable schemes (for positive viscosities) using the time-step predicted by a von Neumann analysis. It was also shown that the div–grad condition is stable only for a significantly smaller time-step.

The div–grad and the curl–curl conditions as well as a homogeneous Neumann condition have also been evaluated in the Navier–Stokes solver OverBlown to study the unsteady flow around cylinders in a 2-D channel. Here the problem was integrated in time with a second order Adams–Bashforth/Adams–Moulton predictor–corrector scheme for the convective part coupled to a second-order Crank–Nicholson scheme for the viscous part. While all three pressure boundary conditions were shown to be second-order accurate, the stability properties were significantly different. In agreement with the analysis and the amplification factor computation, the div–grad condition was only stable for a time-step $\Delta t \leq Ch^2$. In contrast, the curl–curl condition and the homogeneous Neumann conditions were stable for the time-step predicted by a von Neumann analysis based on only the convective terms. Furthermore, it has been demonstrated that the use of the homogeneous Neumann condition leads to significant errors close to no-slip boundaries, which adversely affects the accuracy of integrated quantities such as lift, drag, and torque, which are of utmost importance in engineering applications.

ACKNOWLEDGMENTS

The author thanks Dr. Bill Henshaw for interesting discussions on the present subject and for help with the OverBlown solver. The author is also grateful to Mr. Lars Carlsson for carefully reading the manuscript as well as validating the Matlab code used in Section 4. This work was performed under the auspices of the U.S. Department of Energy by the University of California Lawrence Livermore National Laboratory under Contract W-7405-Eng-48.

REFERENCES

1. J. B. Bell, P. Colella, and H. M. Glaz, A second-order projection method for the incompressible Navier–Stokes equations, *J. Comput. Phys.* **85**, 257 (1989).
2. G. Chesshire and W. D. Henshaw, Composite overlapping meshes for the solution of partial differential equations, *J. Comput. Phys.* **90**(1), 1 (1990).
3. P. M. Gresho and R. L. Sani, On the pressure boundary conditions for the incompressible Navier–Stokes equations, *Int. J. Numer. Meth. Fluids* **7**, 1111 (1987).
4. B. Gustafsson, H.-O. Kreiss, and J. Oliger, *Time Dependent Problems and Difference Methods* (Wiley–Interscience, New York, 1995).
5. W. D. Henshaw, A fourth-order accurate method for the incompressible Navier–Stokes equations on overlapping grids, *J. Comput. Phys.* **113**, 13 (1994).
6. W. D. Henshaw, *OverBlown: A Fluid Flow Solver for Overlapping Grids, Reference Guide*, Research Report UCRL-MA-134289 (Lawrence Livermore National Laboratory, Livermore, CA, 1999).
7. G. E. Karniadakis, M. Israeli, and S. A. Orszag, High-order splitting methods for the incompressible Navier–Stokes equations, *J. Comput. Phys.* **97**, 414 (1991).

8. J. Kim and P. Moin, Application of a fractional-step method to incompressible Navier–Stokes equations, *J. Comput. Phys.* **59**, 308 (1985).
9. K. Z. Korczak and A. T. Patera, An isoparametric spectral element method for solution of the Navier–Stokes equations in complex geometry, *J. Comput. Phys.* **62**, 361 (1986).
10. S. E. Rogers, D. Kwak, and C. Kiris, Steady and unsteady solutions of the incompressible Navier–Stokes equations, *AIAA J.* **29**, 603 (1991).
11. J. C. Strikwerda, Finite difference methods for the Stokes and Navier–Stokes equations, *SIAM J. Sci. Stat. Comput.* **5**(1), 56 (1984).
12. J. C. Strikwerda, High-order-accurate schemes for incompressible viscous flow, *Int. J. Numer. Meth. Fluids*, **24**, 715 (1997).